

# Probing Nanoscale Schottky Barrier Characteristics at WSe<sub>2</sub>/Graphene Heterostructures via Electrostatic Doping

Filipe Richheimer, Tom Vincent, Alessandro Catanzaro, Nathaniel J. Huáng, Mark A. Baker, Robert A. Dorey, Cristina E. Giusca, Fernando A. Castro, Olga Kazakova, and Sebastian Wood\*

The adoption of 2D transition metal dichalcogenide (TMD) based optoelectronic devices is limited by Fermi level pinning effects and consequent large contact resistances upon contacting TMDs with bulk metal electrodes. A potential solution for near-ideal Schottky-Mott behavior and concomitant Schottky barrier height control is proposed by contacting TMDs and (semi-)metals in van der Waals heterostructures. However, measurement approaches to directly assess interface parameters relevant to the Schottky-Mott rule on a local scale are still lacking. In the present work, a heterostructure of monolayer tungsten diselenide (WSe2) with monolayer graphene (1LG) and bilayer graphene (2LG) is investigated on a bottom-gate substrate. Kelvin probe force microscopy and tip-enhanced photoluminescence measurements at different electrostatic doping induced Fermi levels in graphene enable decoupling and quantification of contributions from the interface dipole and electrode work function. These are used to locally probe Schottky barrier characteristics with below 32 nm lateral resolution, demonstrating that the WSe₂/1LG junction operates at the Schottky–Mott limit (S ≈ 1). At the WSe<sub>2</sub>/2LG junction, a reduction of the interface dipole is directly related to changes in excitonic emission properties. These are attributed to charge transfer modulation across the interface, critical for obtaining highperformance transfer characteristics in transistors and related devices.

#### 1. Introduction

In their bulk form, transition metal dichalcogenide (TMD) crystals are indirect bandgap semiconductors composed of

F. Richheimer, T. Vincent, A. Catanzaro, N. J. Huáng, C. E. Giusca, F. A. Castro, O. Kazakova, S. Wood
National Physical Laboratory
Teddington, Middlesex TW11 0LW, UK
E-mail: sebastian.wood@npl.co.uk
F. Richheimer, M. A. Baker, R. A. Dorey
Centre for Engineering Materials
University of Surrey
Guildford GU2 7XH, UK

The ORCID identification number(s) for the author(s) of this article can be found under https://doi.org/10.1002/aelm202200196.

© 2022 National Physical Laboratory. Advanced Electronic Materials published by Wiley-VCH GmbH. This is an open access article under the terms of the Creative Commons Attribution License, which permits use, distribution and reproduction in any medium, provided the original work is properly cited.

DOI: 10.1002/aelm.202200196

vertically stacked X-M-X planes that are weakly bound via van der Waals (vdW) forces.[1] Each plane is formed according to the chemical formula MX<sub>2</sub>, with the M-site being occupied by transition metal atoms and the X-site by chalcogen atoms. When thinned to a 2D monolayer, TMDs (such as M = Mo, W; X = S, Se) become direct bandgap semiconductors. [2-6] The bandgap energies are in the visible to near-infrared range depending on the constituent atoms, which makes these materials attractive for (opto-)electronic devices. Applications of 2D optoelectronic devices include fieldeffect transistors,<sup>[7–9]</sup> photodetectors,<sup>[10–12]</sup> and solar cells.[13-15] Although TMD monolayer channels exhibit excellent properties, forming effective interfaces and good electrical contacts with metal electrodes is challenging. Bulk metal contacts promote Fermi level pinning through dangling crystal terminations as well as defect formation during electrode deposition.[16,17] This leads to strong deviations from the Schottky-Mott limit, characterized by a weak relationship between the Schottky barrier height and metal work function.[18]

Lack of control over the resulting Schottky barriers can lead to high contact resistances with metal electrodes, which are detrimental to device performance characteristics.<sup>[19]</sup> As a result, interfacing bulk metal electrodes with TMDs for low resistance junctions is intrinsically challenging.<sup>[20]</sup>

One approach to improving the contact and the resulting device parameters is to use 2D materials of (semi-)metallic character, typically graphene, as a buffer layer between the TMD channel and bulk metal electrode. [21-25] Here, the vertical assembly of 2D materials results in junctions bound by van der Waals forces and free of interface states due to the absence of dangling bonds at the atomically flat surfaces. In addition, the ability to alter the graphene work function via electrostatic doping enables ambipolar device characteristics as well as controlled Schottky barrier height tuning in graphene/TMD heterostructures.[26,27] Computational studies based on density functional theory (DFT) of these heterostructures have found the electronic structure of the individual layers to be largely preserved upon electrical contact,[28-30] enabling the Schottky barrier to be closely modulated by the doping concentration.



Key to understanding the Schottky barrier height is to unravel the impact on local band structure and Fermi level alignment when a 2D heterostructure of graphene with a TMD is formed. The presence of a band offset was reported by Le Quang et al. employing scanning tunneling spectroscopy, where vertical heterostructures comprised of both MoSe2 and WSe2 were shown to yield a fixed offset between monolayer and bilayer graphene.[31] By employing Kelvin force probe microscopy (KPFM) measurements on similar heterostructures, the band offsets could be directly linked to a fixed work function shift.[32] The work function offsets of TMDs on monolayer and bilayer graphene and the resulting differences in Schottky barrier height were further associated with local variations in photoluminescence spectra, namely local populations of exciton and trion emission.<sup>[33]</sup> Band offsets reported by the aforementioned techniques appear to directly relate to the local charge transfer characteristics, however an understanding of the recorded band offsets in the context of the Schottky-Mott model is still lacking.

In the present work, the electronic landscape of a vdW heterostructure formed out of monolayer and bilayer graphene on a bottom-gate tunable substrate with monolayer WSe<sub>2</sub> on top is investigated. This design allows us to locally separate the effects of the presence of an interface dipole from those of a work function change upon gate modulation expected in an ideal Schottky–Mott contact. We are able to individually assess the electrical contact for monolayer and bilayer graphene and compare it against the Schottky–Mott model. Using graphene work function

modulation via electrostatic doping, this is achieved without having to rely on comparisons between distinct heterostructure regions such as between monolayer and bilayer graphene, as reported in previous work.[31,33] We distinguish a fixed work function offset relative to the underlying graphene, which is attributed to an interlayer charge transfer related interface dipole, from the work function modulation of the heterostructure against the underlying graphene layer, demonstrating a Fermi level pinning free contact. Further, we probe excitonic emission with nanoscale-resolved tip-enhanced photoluminescence spectroscopy (TEPL). We record a gate voltage induced modulation of local exciton and trion populations over a WSe<sub>2</sub>/bilayer graphene region at electrostatic doping regimes when the interface dipole reduces. Our results highlight the importance of disentangling the metal work function and interface dipole contributions in the overall Schottky barrier height and that the latter must be considered to achieve desired interface characteristics. Precise control over the Schottky barrier height is a critical enabler for highly gate-sensitive transfer characteristics.

#### 2. Results

#### 2.1. Heterostructure Characterization

The heterostructure is comprised of a WSe<sub>2</sub> flake transferred onto a 50  $\mu$ m  $\times$  50  $\mu$ m monolayer graphene channel area.

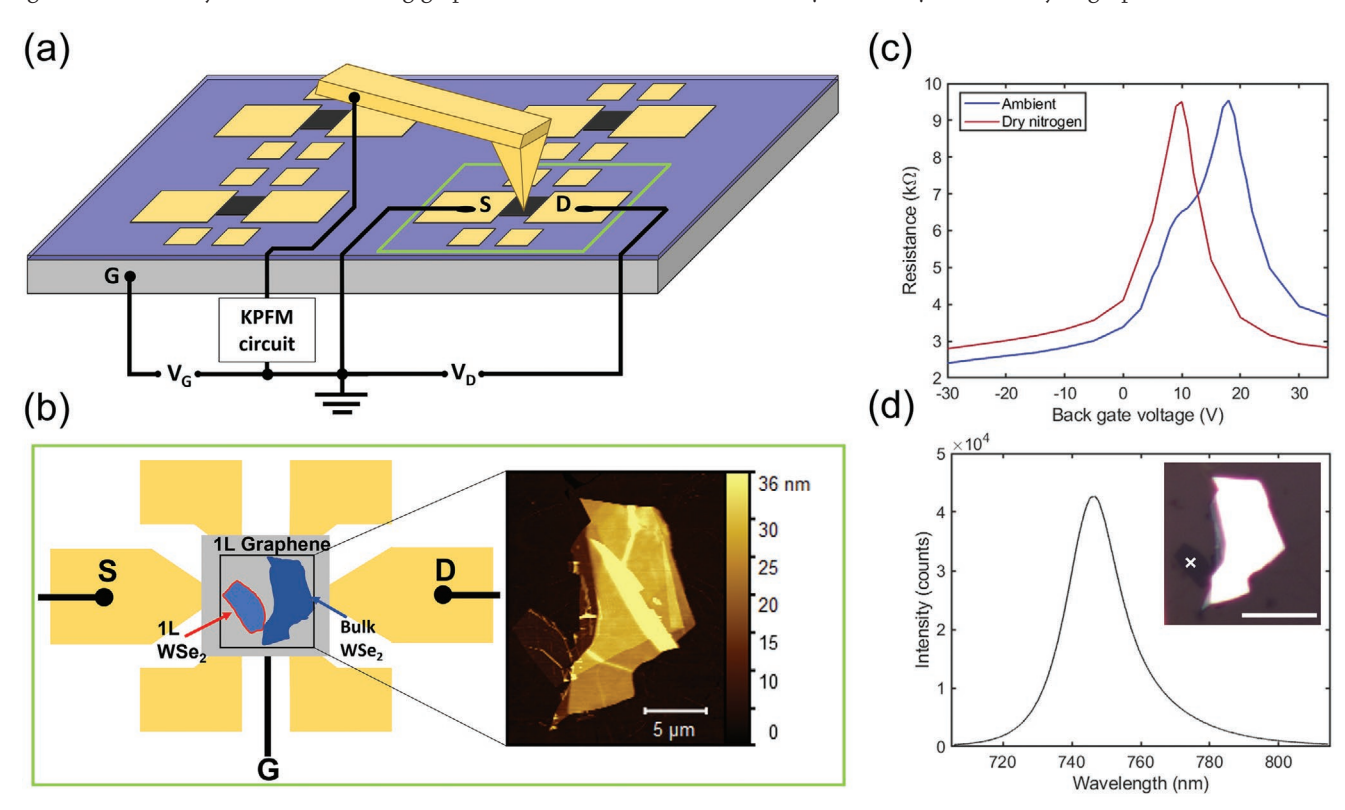


Figure 1. Physical characterization of the WSe<sub>2</sub>/graphene heterostructure. a) Diagram of the sample configuration with source (S), drain (D), and gate (G) contacts together with the KPFM system. b) G-FET element with transferred WSe<sub>2</sub> flake. The WSe<sub>2</sub> flake (blue) is situated on the graphene channel (gray). Inset shows atomic force microscopy image of WSe<sub>2</sub> flake. The monolayer WSe<sub>2</sub> is located on the left of the flake. c) Source–drain resistance against gate voltage of graphene channel taken inside and outside dry nitrogen filled glovebox. d) PL spectrum on monolayer WSe<sub>2</sub> region. Inset shows optical microscopy image with cross indicating the region where the PL spectrum was acquired. The scale bar represents 10 μm.





The geometry and layout of the 2D heterostructure are shown in Figure 1a,b. The substrate contains several individual graphene field-effect transistor (G-FET) devices as illustrated in Figure 1a. Here, to simultaneously perform KPFM measurements and induce electrostatic doping of the graphene channel via gate voltage tuning, the source contact was grounded. The drain contact (which was grounded during KPFM measurements) was connected separately to the source pad for channel resistance measurements. Each G-FET element is composed of six gold pads contacting the channel, as illustrated in Figure 1b. The four contacts arranged along the top and bottom of the monolayer graphene enable Hall-type measurements and were not electrically connected in the current experiment. The two lateral contacts were wire bonded to larger contact pads and used as source and drain contacts. A gate contact was established by electrically connecting the silicon gate substrate. An atomic force microscopy (AFM) topography scan is shown in Figure 1b, which highlights the overall bulk character of the WSe2 flake (exceeding 10 nm thickness) with a substantially thinner area to the left side of the flake (a few micrometers in size).

The position of the charge neutrality point (CNP) in the G-FET device containing the heterostructure was studied by measuring the source-drain resistance as a function of the applied gate voltage. The density of states has a minimum at the CNP, resulting in a maximum of the channel resistance. The CNP is therefore located by modulating the gate voltage, which leads to a displacement of the work function via electrostatic doping. Figure 1c plots the channel resistance against the applied back-gate voltage recorded inside the glovebox (dry N<sub>2</sub>), as well as in ambient conditions. To measure the channel resistance at ambient conditions, the sample was taken out of the glovebox with inert atmosphere the day before the measurement. The peaks in resistance show that the CNP in the graphene channel is reached at ≈10 and 17 V of applied back-gate voltage when measured in the glovebox and in ambient environment, respectively. A positive gate voltage at the CNP indicates p-type doping of the monolayer graphene at zero gate voltage, with further increased p-type doping under environmental conditions. This suggests that the p-type doping is induced by a combined effect of the graphene/SiO<sub>2</sub> interface<sup>[34,35]</sup> and airborne molecules adsorbed on the free surface. [36] This is reinforced by the characteristics of the resistance curve under ambient conditions, where the additional shoulder at 10 V could reflect the proportion of graphene buried under the WSe2, which shields it from adsorption of airborne molecules.

The monolayer character at the thin section of the WSe<sub>2</sub> flake was probed via photoluminescence (PL) spectroscopy, with a representative spectrum shown in Figure 1d. The spectrum was taken at the position marked by the white cross in the optical microscopy image inset. The highly luminescent spectrum centered at around 745 nm ( $\approx$ 1.66 eV) is characteristic of the neutral exciton emission in WSe<sub>2</sub>, <sup>[37,38]</sup> which is consistent with the direct bandgap emission characteristics of monolayer WSe<sub>2</sub> flakes. The emission peak has an asymmetric tail toward the red end, which is indicative of radiative recombination of trion states. <sup>[39]</sup> Given the interface with the underlying graphene, electron transfer from graphene

toward the  $WSe_2$  is expected, resulting in negatively charged trions. $^{[40,41]}$ 

#### 2.2. Charge Transfer Modulation

The presence of interfacial charge transfer suggested by the asymmetric PL shape (above) was further investigated using KFPM. KPFM measures contact potential difference (CPD), which in our measurements corresponds to the tip surface work function relative to the work function of the sample (see the Experimental Section). Variation in the CPD signal reveals local work function differences due to the amount of charge transfer across the heterostructure interface. The additional application of electrostatic doping via gate bias modulates the local charge transfer and enables us to compare local junction characteristics with the Schottky–Mott rule.

The KPFM measurements of the heterostructure region at different back-gate voltages are shown in **Figure 2**. The region of interest, containing the heterostructure composed of monolayer  $WSe_2$  and monolayer graphene, is shown in Figure 2a. The applied back-gate voltage range was selected according to the CNP identified via channel resistance measurements to lie at 10 V when recorded under identical conditions inside the nitrogen glove box. Thus, KPFM maps were recorded from 0 to 10 V back-gate voltage in 2 V increments as shown in Figure 2b–g.

The KPFM maps in Figure 2b-g are all displayed in a fixed CPD scale to facilitate the visualization of CPD changes with different back-gate voltages. With increasing gate voltage, an overall increase in the CPD of the free monolayer graphene surrounding the surface, as well as of the WSe2/graphene heterostructure, is observed. With KPFM compensating voltages applied to the probe, a recorded CPD increase corresponds with a decrease in sample work function. Here, the work function decreases as the gate bias increases, indicating a modulation of p-type doped graphene towards the CNP, in agreement with the channel resistance measurements. The KPFM results also show a relation between work function modulation and structural disorder. Wrinkles in the WSe2, such as those highlighted by the white arrows in Figure 2a exhibit smaller CPD changes with gate voltage compared to the surrounding areas. This behavior is shown by the cross-section plot in Figure 2h, where the dips in CPD on the heterostructure region that correspond to wrinkles are less separated with increasing gate voltage. We attribute reduced work function modulation at wrinkles to the increased distance between WSe<sub>2</sub> and the underlying graphene, introducing a barrier to Fermi level alignment and charge transfer.

We also observe that structural inhomogeneities in the graphene layer alter the local charge transfer. One example is highlighted by the black arrow in Figure 2g, where a linear feature with lower CPD lies perpendicular to one caused by a WSe<sub>2</sub> wrinkle. As no corresponding topography feature is recorded at the same line position, we identify it as a grain boundary in the CVD graphene monolayer. This is confirmed by the appearance of a visible grain boundary in the graphene film at the high-resolution AFM scan in Figure S1 (Supporting Information). Grain boundaries on graphene are rationalized to yield

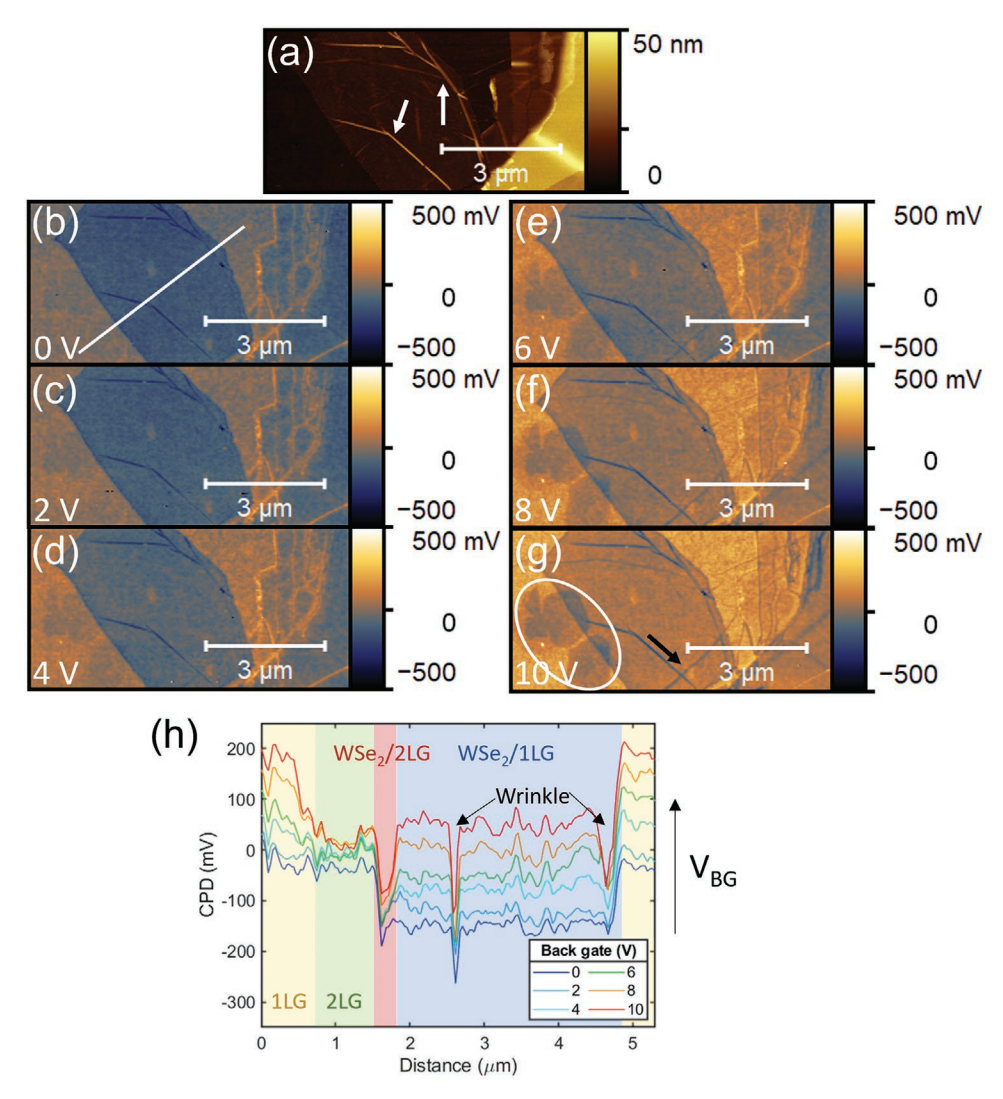


Figure 2. KPFM maps of monolayer WSe<sub>2</sub>/graphene heterostructure during electrostatic doping. a) AFM topography of the investigated heterostructure region with white arrows highlighting structural defects on WSe<sub>2</sub>. b–g) KPFM measurements at heterostructure region recorded at 0–10 V gate bias in 2 V increments. In (g), black arrow highlights subsurface structural defect on graphene, and white ellipse contains bilayer graphene regions. h) Cross section of contact potential difference (CPD) variation extracted along the white line shown in (b).

greater CPD variations close to the CNP as the lower density of states inhibits screening effects.<sup>[34]</sup> Similarly, as the gate bias increases, two islands of low CPD values appear at the left edge of the flake—these are clearly visible in Figure 2e–g (see white ellipse in Figure 2g) but indistinguishable in Figure 2a. These islands were identified as AB stacked bilayer graphene by comparing their Raman spectra with the surrounding graphene (Figure S2, Supporting Information).<sup>[42]</sup> The bilayer graphene also shows smaller CPD changes with gate voltage according to Figure 2g, which is due to differences in the density of states compared to monolayer graphene.

To quantify the differences in work function modulation by electrostatic doping in heterostructures formed between monolayer  $WSe_2$  and either monolayer  $WSe_2/1LG$ ) or bilayer graphene  $WSe_2/2LG$ , we evaluated the mean CPD values of the respective areas. When computing the mean and standard deviation of spatial areas, each pixel was assumed to represent an independent measurement. When the lateral spacing between

pixels is larger than the lateral resolution of the measurement, neighboring points do not contain overlapping information, thus classifying as independent measurements. A cross section extracted along a WSe $_2$  flake edge in Figure S3 (Supporting Information) is used to demonstrate that the spatial resolution is smaller than the selected step size of  $\approx 32$  nm.

**Figure 3** shows the mean of extracted spatial areas with uncertainty given by the standard deviation and assuming a normal distribution using a coverage factor of 1. The cases of monolayer and bilayer graphene were plotted separately in Figure 3a,b, respectively. Comparing the blue points in each figure shows that the CPD values for exposed monolayer and bilayer graphene regions scale differently with applied electrostatic doping (gate bias). This can be ascribed to the differences in charge carrier density (n) variation with Fermi level across the CNP. For monolayer graphene the Fermi level varies as  $\sqrt{n}$ , with n being the carrier concentration, leading to an S-shape with inflection point at the CNP. [43] In bilayer graphene, the



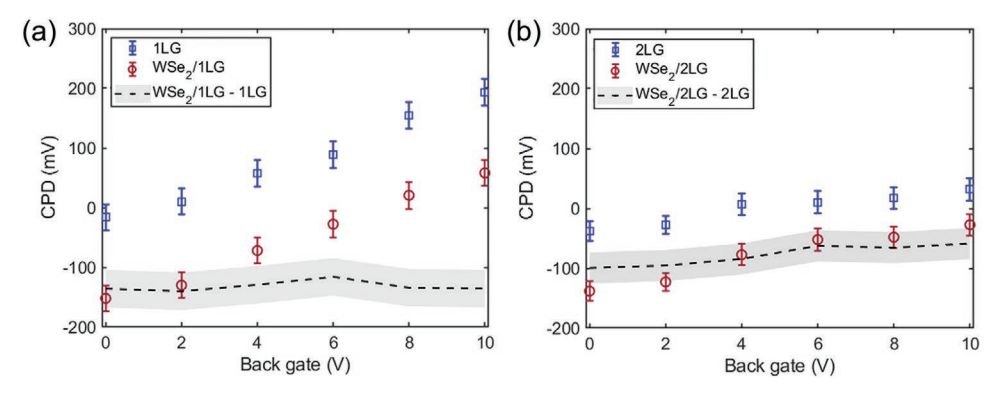


Figure 3. CPD variation against applied back-gate voltage for selected sample areas. a) Comparison of CPD evolution between exposed monolayer graphene (ILG, blue), heterostructure of monolayer WSe<sub>2</sub> with monolayer graphene (WSe<sub>2</sub>/1LG, red), and difference between heterostructure and monolayer graphene (WSe<sub>2</sub>/1LG– 1LG, black). b) CPD evolution of bilayer graphene (2LG, blue), heterostructure of monolayer WSe<sub>2</sub> with bilayer graphene (WSe<sub>2</sub>/2LG, red), and difference between respective heterostructure and bilayer graphene (WSe<sub>2</sub>/2LG– 2LG, black).

carrier density is modeled according to a 2D electron gas and thus scales linearly  $(\infty n)$  with the Fermi level. [43] The work function on the heterostructures largely follows the trend of the underlying monolayer or bilayer graphene, as previously predicted by DFT simulations. [44] To understand the backgate modulation of the CPD at the heterostructure relative to the exposed graphene, the difference between the CPD on the heterostructure and its exposed graphene counterpart was evaluated and plotted in each figure corresponding to the black dotted lines. The uncertainty was propagated as the square root of the sum of the squared uncertainties between the CPD at the heterostructure and the corresponding exposed graphene at each gate bias and is represented by the gray shaded area.

The CPD measured for the WSe<sub>2</sub>/graphene heterostructure is persistently lower than that of the exposed graphene surface, which is consistent with charge transfer between graphene and the WSe<sub>2</sub>, as previously inferred from the presence of trion emission. In the WSe<sub>2</sub>/1LG heterostructure, the CPD difference maintains a constant offset of around –135 meV. A monotonic increase (decrease in absolute value) in CPD offset ( $\Delta$ CPD = CPD<sub>heterostructure</sub> – CPD<sub>graphene</sub>) is observed for the WSe<sub>2</sub>/2LG heterostructure, where the  $\Delta$ CPD starts at close to –100 meV at 0 V back-gate voltage and reaches  $\approx$ –60 meV at 10 V back-gate voltage.

#### 2.3. Optical Response to Modulation

To investigate the impact of back-gate induced charge transfer towards exciton populations, spatially resolved PL was employed. The size of the bilayer graphene islands is comparable to the length scale of the optical diffraction limit, so tipenhanced PL (TEPL) spectroscopy was used to resolve these features. Here, by irradiating the apex of a metal-coated AFM probe, the excitation of a localized surface plasmon resonance (LSPR) results in spatial confinement of the optical excitation into a near-field volume on the nanometer scale. [45–47] TEPL was measured on a  $1\,\mu\text{m}\times1\,\mu\text{m}$  area (40  $\times$  40 pixels) capturing vdW heterostructures with both monolayer and bilayer graphene. At each pixel, a spectrum was acquired by using a dual acquisition and computing the spectrum difference to isolate the near-field

component of the signal, further details can be found in the Experimental Section.

The TEPL measurements were carried out with 0 and 10 V gate bias to match the graphene CNP position. These results are displayed in Figure 4a,b, respectively. Each pixel represents the integrated area under the TEPL emission spectrum. The false color intensity scale was kept fixed across maps to facilitate the visualization of changes between applied backgate voltages. Specifically, the measured region corresponds to the large wrinkle where the WSe2 meets the flake edge, which is further highlighted in Figures S1 and S4 (Supporting Information). In Figure 4a, the area of the WSe<sub>2</sub>/2LG heterostructure is visible due to the reduced emission intensity around the upper left side of the image. Between Figure 4a,b, an overall decrease in the TEPL emission intensity is recorded predominantly on the region containing bilayer graphene (top left quadrant of the plot). The evolution of the TEPL emission was further studied with back-gate voltages of -20 and 20 V as shown in Figure S5 (Supporting Information). These measurements confirm the emergence of a sharp decrease in emission intensity for gate biases between 0 and 10 V, with less substantial changes between TEPL maps at -20 and 0 V as well as between 10 and 20 V. The abrupt transition in emissive properties on the WSe2/2LG region between 0 and 10 V gatebias thus falls in the same range as the previously recorded  $\Delta$ CPD increase.

To evaluate the spectral changes more closely, a set of averaged spectra at regions of WSe<sub>2</sub>/1LG and WSe<sub>2</sub>/2LG vdW heterostructures were extracted inside the dashed rectangles. The positions of the rectangles are slightly offset between Figure 4a and Figure 4b, in an attempt to compensate a lateral drift between images as seen in Figure S5 (Supporting Information). In Figure 4c, spectra extracted from the WSe<sub>2</sub>/1LG region were compared for 0 and 10 V gate bias, showing no appreciable changes due to electrostatic doping. In contrast, for the WSe<sub>2</sub>/2LG region shown in Figure 4d, a substantial quenching of the PL emission is measured with applied back-gate bias (10 V), together with a slight redshift of 4 nm in the spectrum. The redshift is further seen in the inset, where the peak intensities were normalized, showing an enhanced low energy tail for the spectrum extracted at 10 V gate bias. Quenching and

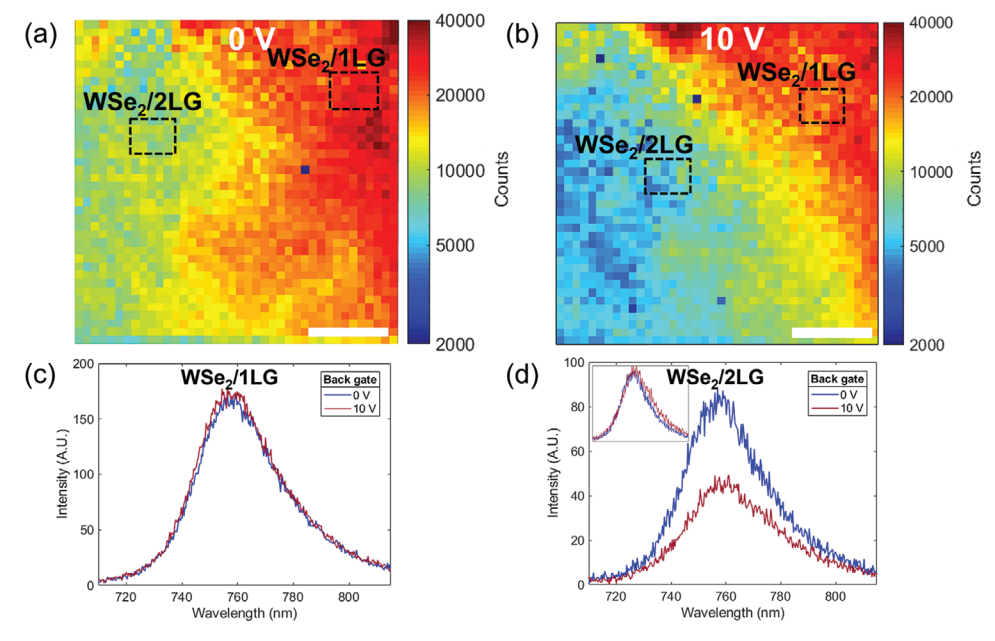


Figure 4. TEPL investigation of region containing WSe<sub>2</sub>/1LG and WSe<sub>2</sub>/2LG vdW heterostructures. TEPL maps integrated across full spectrum with a) 0 V and b) 10 V back-gate voltage. Selected spectral regions averaged inside dashed rectangles in (a) and (b) plotted for c) WSe<sub>2</sub>/1LG and d) WSe<sub>2</sub>/2LG. d) Further contains inset of normalized spectra at 0 and 10 V back-gate voltage. Scale bars in (a) and (b) denote 250 nm.

redshift of the PL spectrum in a back-gated WSe<sub>2</sub>/1LG heterostructure is attributed to interlayer charge transfer, with increased redshift and quenching denoting a larger proportion of trion emission.<sup>[40]</sup>

# 3. Discussion

### 3.1. Quantifying Electrostatic Doping on Graphene

The macroscopic graphene channel resistance measurements located the graphene CNP at an applied back-gate voltage of around 10 V, identifying the graphene as naturally p-type doped in the absence of a gate bias. The resulting charge carrier density variation (n) due to electrostatic doping can be obtained by using a plate capacitor model with  $n = \alpha (V_G - V_G^{CNP})$ , [48] where  $V_{\rm G}$  and  $V_{\rm G}^{\it CNP}$  are the applied gate voltage and the gate voltage needed to reach the CNP, respectively. The geometric capacitance coefficient  $\alpha = \varepsilon_r \varepsilon_0/ed$  is determined by replacing the dielectric constant of the  $SiO_2$  gate dielectric  $\varepsilon_r = 3.9$  as well as the gate dielectric thickness of d = 90 nm, whilst e and  $\varepsilon_0$ are the elemental charge and vacuum permittivity constants, respectively. Thus, at 0 V back-gate voltage an adjusted carrier density of  $n = -2.4 \times 10^{12}$  cm<sup>-2</sup> on monolayer graphene is obtained, where the negative sign denotes hole doping. The carrier density induced in graphene by electrostatic doping is expected to be widely modeled by the geometric capacitance, with little contribution from the quantum capacitance.<sup>[49]</sup>

The estimated doping density relative to the CNP from the capacitor model can be converted into a Fermi level ( $E_F$ ) in monolayer graphene with the expression<sup>[50,51,52]</sup>

$$E_{\rm F} = \pm \, \hbar \nu_{\rm F} \sqrt{\pi \, |n|} \tag{1}$$

Here, the  $\pm$  sign is positive/negative for electrons/holes,  $\hbar$  is the reduced Planck constant, and  $v_F$  the Fermi velocity, which for monolayer graphene on a SiO2 substrate has an estimated value of  $v_F = 1.1 \times 10^6$  m s<sup>-1.[53]</sup> Inserting the carrier density of  $n = 2.4 \times 10^{12} \text{ cm}^{-2}$  at 0 V (see above) yields an estimated Fermi level offset of  $E_{\rm F} = -198$  meV. From Figure 3a, the Fermi level shift for monolayer graphene corresponding to gate bias decreasing from 10 to 0 V is measured at  $-210 \text{ meV} \pm 31 \text{ meV}$ , which is in good agreement with the predicted carrier density through electrostatic doping. This compatibility between experimental (KFPM) and theoretical determination of Fermi level position (based on well-known material properties and the macroscopic CNP measurement) supports the use of frequency modulation (FM-)KPFM for quantitative evaluation of local work function. [54-57] Using the linear relationship between Fermi level and carrier density for bilayer graphene<sup>[58]</sup> (which otherwise only shows a dependency with the effective carrier mass), the carrier density resulting from electrostatic doping can be estimated using the Fermi level values obtained by KPFM. Using an effective carrier mass of  $m_{\text{eff}} = 0.033 \, \text{m}_{\text{e}}$ , [59] where  $m_{\rm eff}$  is the electron rest mass, the total carrier density difference between 0 and 10 V back-gate voltages is estimated at  $|\Delta n| = 1.94 \times 10^{12} \text{ cm}^{-2}$ . In contrast to monolayer graphene, the CNP of the bilayer graphene islands is unknown and could lie inside or outside the investigated gate bias range. As undoped (at CNP) monolayer and bilayer graphene work functions have been measured to lie at 4.57 eV  $\pm$  0.05 eV and 4.69 eV  $\pm$  0.05 eV, respectively,[58] and considering the measured CPD of monolayer graphene as an accurate reflection of its CNP, it is expected that bilayer graphene remains p-doped throughout the investigated back-gate voltage range. On this basis, the work function changes during electrostatic doping for exposed monolayer and bilayer graphene are illustrated in Figure S6 (Supporting Information).

219910x, 2022, 9, Downloaded from https://onlinelibrary.wiley.com/doi/10.1002/aelm.202200196 by Test, Wiley Online Library on [31/10/2022]. See the Terms and Conditions (https://onlinelibrary.wiley.com/ems-and-conditions) on Wiley Online Library for rules of use; OA articles are governed by the applicable Creative Commons Licensea and Conditions (https://onlinelibrary.wiley.com/ems-and-conditions) on Wiley Online Library for rules of use; OA articles are governed by the applicable Creative Commons Licensea and Conditions (https://onlinelibrary.wiley.com/ems-and-conditions) on Wiley Online Library for rules of use; OA articles are governed by the applicable Creative Commons Licensea and Conditions (https://onlinelibrary.wiley.com/ems-and-conditions) on Wiley Online Library for rules of use; OA articles are governed by the applicable Creative Commons Licensea and Conditions (https://onlinelibrary.wiley.com/ems-and-conditions) on Wiley Online Library for rules of use; OA articles are governed by the applicable Creative Commons Licensea and Conditions (https://onlinelibrary.wiley.com/ems-and-conditions) on Wiley Online Library for rules of use; OA articles are governed by the applicable Creative Commons Licensea and Conditions (https://onlinelibrary.wiley.com/ems-and-conditions) on Wiley Online Library for rules of use; OA articles are governed by the applicable Creative Commons Licensea and Conditions (https://onlinelibrary.wiley.com/ems-and-conditions) of the conditions of the condit

# ADVANCED ELECTRONIC MATERIALS WAYN Adveloctronic mat de

#### 3.2. Interlayer Charge Transfer

When graphene and WSe2 are contacted, electron transfer from graphene to WSe2 occurs, as identified by our experimental results and predicted by DFT simulations in literature.[32] The charge transfer aligns the Fermi level equilibrium and concomitantly leads to a rearrangement of the vacuum levels. The rearrangement is achieved via a vertical interface dipole forming across 2D layers, as opposed to band bending in bulk junctions. The magnitude of the interface dipole is influenced by the work function difference of each material comprising the heterostructure as well as the resulting interlayer separation distance governed by the Pauli exclusion principle.<sup>[60,61]</sup> In our KPFM measurements on the WSe<sub>2</sub>/graphene heterostructure, a negative CPD offset of around -135 meV was recorded relative to the exposed (monolayer) graphene. The negative offset in Figure 3b in the absence of a gate bias reflects a fixed offset for both monolayer and bilayer graphene heterostructures relative to the uncovered graphene films within the uncertainty of the measurement. This CPD offset evidences the presence of an interface dipole and concomitant potential step in the vacuum energy  $\Delta V$ , driven by interlayer charge transfer when both layers are contacted. Accounting for the interface dipole, the resulting Schottky barrier for electrons and holes, respectively, can be written as<sup>[62,63]</sup>

$$\Phi_{B,n} = W_G - \chi_{WSe_2/G} + \Delta V \tag{2}$$

$$\Phi_{\text{B,p}} = -\left(W_{\text{G}} - I_{\text{WSe}_{\gamma}/\text{G}} + \Delta V\right) \tag{3}$$

Here,  $W_G$  is the graphene work function, and  $\chi_{WSe_2/G}$  and  $I_{WSe_2/G}$  are the electron affinity and ionization potential of the vdW heterostructures, respectively, between  $WSe_2$  and graphene. By attributing the  $\Delta CPD$  measured in Figure 3 to the interface dipole, the entire work function difference at the heterostructure is absorbed by the  $\Delta V$  term with respect to the exposed graphene. In reality, we may expect the underlying graphene at the heterostructure to undergo a work function shift when contacted with  $WSe_2$ . However, we expect this effect to be reasonably small, since the interface dipole remains constant for monolayer graphene as shown in Figure 3a. This would not be expected if the buried graphene in the  $WSe_2/1LG$ 

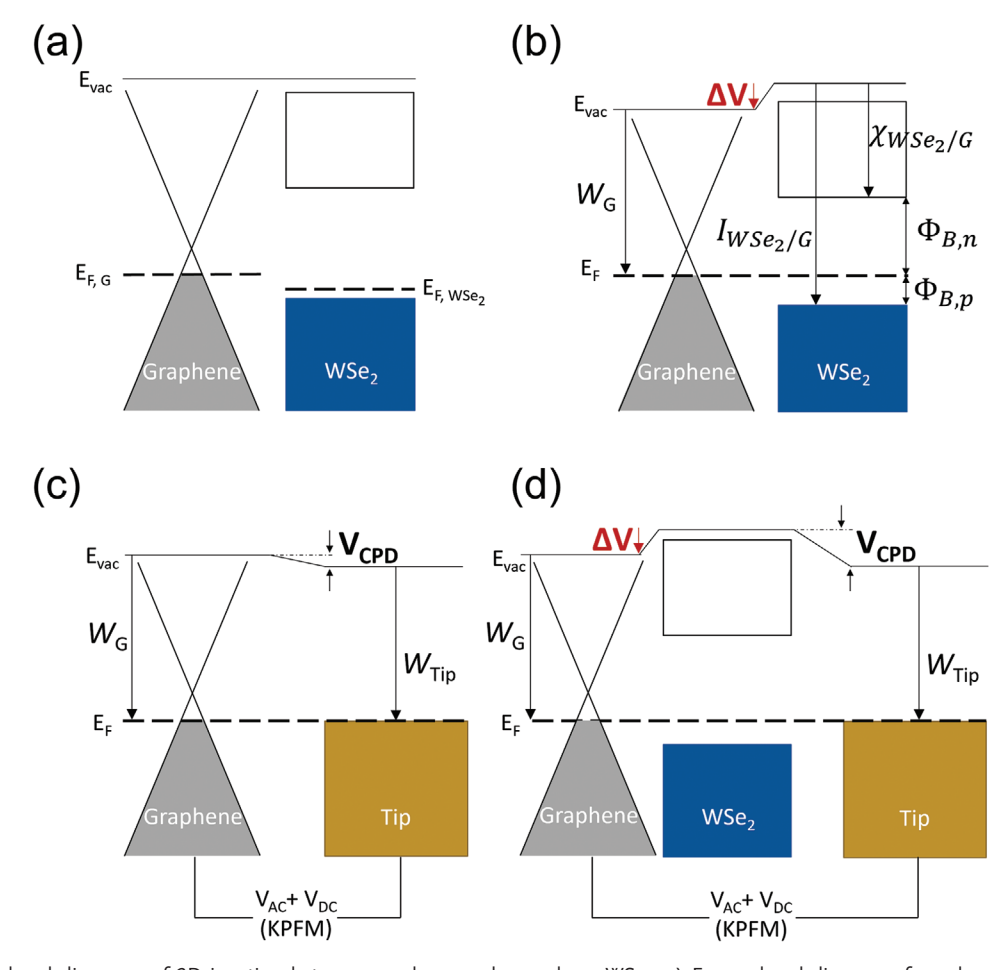


Figure 5. Energy band diagrams of 2D junction between graphene and monolayer WSe<sub>2</sub>. a) Energy band diagram of graphene and WSe<sub>2</sub> prior to establishing electrical contact. b) Energy band diagram after contacting graphene and WSe<sub>2</sub>, characterized by the formation of a sharp interface dipole  $\Delta V$  across the vdW gap and a Schottky-type contact. Schematics in (c) and (d) illustrate KPFM measurements on graphene and WSe<sub>2</sub>/graphene heterostructure.





heterostructure had a substantially different work function relative to the exposed graphene, and thus would reach the CNP at a different gate voltage.

The link between the electronic band structures and the KPFM measurements is further established via the schematic in Figure 5. Prior to being brought into contact, the energy levels of the WSe<sub>2</sub> monolayer of p-type character (see the Experimental Section) and graphene are illustrated in Figure 5a. Once brought into contact, the vacuum level offset is characterized by the formation of an interface dipole  $\Delta V$  across the vdW gap from WSe2 toward graphene and a Schottky-type contact emerges (Figure 5b). During KPFM measurements, the additional presence of the Au-coated AFM tip and its work function has to be taken into account. The band alignments between graphene and the KPFM tip as well as the vdW heterostructure with the KPFM tip contacted to the graphene are displayed in Figure 5c,d, respectively. On bare graphene, the DC bias required to compensate the local CPD is given directly by the difference between the tip work function  $(W_{Tip})$  and graphene work function  $(W_G)$ . When measured on the vdW heterostructure, a vacuum level increase by  $\Delta V$  will have to be additionally compensated via the DC bias. In the absence of parasitic effects, the recorded CPD of exposed graphene and the heterostructure should differ by the potential induced due to the interface dipole. Under these circumstances it follows that the  $\Delta$ CPD plots (black lines) in Figure 3a,b act as a direct measure of the interface dipole.

Following the interpretation of the junction characteristics accessible via KPFM, we can use these to consider the extent of Fermi level pinning at the vdW heterostructure. The presence/ absence of Fermi level pinning is typically assessed via the interface parameter S, which evaluates the dependency of the Schottky barrier height  $\Phi_B$  with the electrode work function (in our case, graphene)  $W_G$  by  $S = d\Phi_B/dW_G$  in the Schottky–Mott theory. As  $\Delta V$ ,  $\chi_{\rm WSe_2/G}$ , and  $I_{\rm WSe_2/G}$  in Equations (2) and (3) are all constants in relation to W<sub>G</sub>, we used the data in Figure 3a to calculate  $S \approx 1$  (see Figure S7, Supporting Information). This result represents a WSe2/G heterojunction interface with negligible Fermi level pinning. Employing conventional bulk metal electrodes to contact WSe2, interface parameters of 0.25 to 0.38 are reported. [64,65] Therefore, the results presented in this paper represent a three- to fourfold increase in modulation of Schottky barrier height relative to standard metal electrodes. A greater control over the Schottky barrier height allows engineering devices with reduced contact resistances as well as ambipolar carrier injection while using the same electrode material.

In the absence of applied gate bias, the vdW heterostructure with bilayer graphene yields a comparable interface dipole as the WSe<sub>2</sub>/1LG heterostructure, according to Figure 3b, suggesting similar absence of Fermi level pinning. This observation is consistent with recent studies investigating the local interface properties of heterostructures between WSe<sub>2</sub> and epitaxial graphene containing regions of monolayer and bilayer graphene. There, a Fermi level pinning free interface was largely inferred from the Fermi level shift of the respective heterostructures displaying the same energy shift as the underlying monolayer and bilayer graphene. In the present work, Fermi level pinning is locally studied on the same structure via

independently modulating the graphene work function at multiple doping levels. This approach excludes any parasitic effects such as a variation in equilibrium distance between  $WSe_2$  and monolayer/bilayer graphene, which is known to impact the magnitude of the interface dipole. [63]

Finally, the modulation of the work function of the underlying graphene further revealed a reduction of the interface dipole between bilayer graphene and WSe2. The magnitude of the interface dipole reduces by  $\approx\!40$  meV as the back-gate voltage increases from 0 to 10 V, evidencing a decrease in vacuum level offset. This reduction in the magnitude of the interfacial dipole is supported by the TEPL measurements, which showed strong quenching of the emission spectrum at 10 V back-gate bias along with a relative enhancement of the lowenergy tail (Figure 4d). This can be understood in terms of a reduced potential barrier to interlayer charge transfer for photogenerated excitons resulting in non-radiative interlayer relaxation as well as a relative enhancement of trion emission.  $^{[40]}$ 

As the interface dipole is driven by the electronic structure of the constituent 2D materials and the equilibrium interlayer distance, the observed reduction in interface dipole is most likely driven by a change in one of those parameters. Importantly, the effects associated with a reduction in interlayer dipole strength were only observed for the vdW heterostructure with bilayer graphene. The interface dipole of the WSe<sub>2</sub>/1LG heterostructure did not exhibit this effect and was measured simultaneously, so instrumental artifacts are excluded. Local differences in band alignment and PL emission had been observed for monolayer and bilayer graphene vdW heterostructures with WS2 at fixed electronic configurations.[33] These results suggest that transfer characteristics of optoelectronic WSe<sub>2</sub>/2LG devices would yield greater sensitivity in the investigated gate bias range compared to 1LG counterparts. Such control of the transfer characteristics via dipole layers has been successfully realized in other material systems.[66,67]

# 4. Conclusion

We studied the interface properties of vdW heterostructures between monolayers and bilayers of graphene and a monolayer of WSe2 as a function of electrical doping modulation through bottom-gate biasing. Spatially resolving work function variations at different gate voltages via KPFM, we achieved lateral resolutions below 32 nm. Together with macroscopic channel resistance measurements, we attributed an initial p-type doping of ≈200 meV below the CNP in the absence of gate voltage to monolayer graphene, reaching the CNP with 10 V applied gate voltage. We showed evidence of an ideal Schottky-Mott behavior and subsequent absence of Fermi level pinning in graphene/ WSe<sub>2</sub> heterostructures by comparing the work function modulation at the heterostructures relative to the surrounding freestanding graphene during electrostatic doping. A fixed interface dipole larger than -100 meV relative to the free graphene was recorded that contributed toward the Schottky barrier height at the interface. Over the gate voltage range studied, we recorded ideal Schottky-Mott character for heterostructures with monolayer graphene, whilst bilayer graphene showed two distinct regimes. When electrostatically gate-biasing up to 4 V, we



measured heterostructures with bilayer graphene to closely track the work function of surrounding exposed bilayer graphene. For gate bias between 4 and 10 V, the interface dipole reduced by more than 40 meV. These changes in electronic properties were consistent with nanoscale tip-enhanced optical photoluminescence measurements presented. While photoluminescence spectra remained unchanged on the WSe<sub>2</sub> heterostructures with monolayer graphene under the surveyed gate voltages, a substantial quenching and increased low energy emission tail was recorded for the heterostructure with bilayer graphene.

The obtained results highlight the importance of combined local nanoscale resolved investigation of electronic and optical properties to gain insight into the charge transfer effects and the impact on charge relaxation pathways. The methodologies and conclusions developed in the present work are applicable to a wide range of 2D vdW heterostructures. The benefit of using work function modulation to the metallic 2D layer in a metalsemiconductor vdW heterostructure is highlighted by being able to monitor changes in interface dipole revealed under an applied gate voltage. As demonstrated in the present work, the assessment of the Schottky barrier height via the relative work functions, which is critical for parameters such as device transfer characteristics, is insufficient and changes in interface dipole need to be considered. Increased charge transfer recorded at heterostructures with bilayer graphene suggests the ability to form highly sensitive devices by manipulating the Schottky barrier height via the interface dipole, which impacts critical device properties such as transfer characteristics.

# 5. Experimental Section

 $WSe_2/Graphene$  Heterostructure: The monolayer graphene field effect transistor (G-FET) device deposited by chemical vapor deposition (CVD) was acquired from Graphenea Inc. (GFET-S10). The graphene was contacted by patterned Au/Cr electrodes for source and drain contacts, with the gate substrate formed of doped silicon separated from the graphene channel by a 90 nm thick  $SiO_2$  gate dielectric. Before  $WSe_2$  transfer, the as purchased G-FET device was cleaned by submerging in an acetone bath for at least 12 h. The  $WSe_2$  monolayer was prepared by exfoliation from a p-type bulk crystal (HQ graphene) onto a polydimethylsiloxane (PDMS) film, followed by transfer onto a G-FET channel device via viscoelastic stamping. The micrometer-accuracy alignment between the PDMS film and the G-FET was performed using a home-made microactuator positioning system. The sample was continuously stored in a glovebox environment under dry nitrogen conditions.

Channel Resistance Measurements: Measurements of the graphene channel resistance as a function of gate voltage were performed with a two-channel source/measure unit (Keysight B2921A, Keysight Technologies), recording the source—drain current under constant 10 mV bias applied on one channel, while incrementing the gate—source voltage on the other separate channel.

Atomic Force Microscopy: AFM measurements were performed on a sample scanner system (Combiscope 1000, AIST-NT). The system was incorporated in a glovebox system with controlled inert  $N_2$  atmosphere (Jacomex GP(Concept) T2 4385), keeping oxygen gas and  $H_2\text{O}$  levels below 1 ppm. Gold-coated probes of force modulation type with nominal resonant frequency of 70 kHz and force constant of 2 N  $\text{m}^{-1}$  were used (OPUS 240AC-GG, MikroMasch) and topography recorded by keeping the oscillation amplitude at the first cantilever eigenmode constant with height displacement.

Kelvin Probe Force Microscopy: KPFM measurements were run in parallel with AFM inside the same glovebox. KPFM was operated in dual-pass frequency modulation (FM-)KPFM to minimize the impact

of stray fields induced by the gate bias and give high lateral resolution. Here, in the first pass topography was recorded equivalent to the process described in the previous AFM section. During the second pass, the Au-coated probe tracked the topography signal recorded during the first pass at a lift height of 10 nm, while being mechanically driven at the resonant frequency ( $f_{\rm res} \approx 70$  kHz) and an additional lower frequency AC voltage applied to the tip ( $f_{\rm AC} = 512$  Hz). The FM-KPFM feedback loop was set at the first intermodulation product ( $f_{\rm res} \pm f_{\rm AC}$ ), where a DC voltage was applied to compensate the local contact potential difference. [69] With the voltages related to the KPFM feedback loop applied to the probe, the measured CPD is given by the difference between tip and sample work functions, CPD = ( $W_{\rm tip} - W_{\rm sample}$ )/e. [70]

Tip-Enhanced Photoluminescence Spectroscopy: TEPL spectroscopy measurements were performed on the same scanning probe microscopy platform as KPFM. Probes for TEPL were made by thermal evaporation of a plasmonic coating. Here, silicon force-modulation type probes with 85 kHz nominal resonant frequency and 2.8 N m<sup>-1</sup> force constant (ATEC-FM, NANOSENSORS) were used. Initially a thermal oxide was grown (≈300 nm thickness) in a tube furnace at 1000 °C for 45 min under continuous water vapor flow. The probes were subsequently exposed to a UV-ozone cleaning treatment for 45 min (T10×10/OES/E, UVOCS) before loading inside the thermal evaporator (LABmaster SP/DP, MBRAUN). A purpose-built probe holder system was designed to ensure the tip axis is maintained at the optimum angle to the plane of the evaporator source. Silver wire with 99.9999% purity (Agar Scientific) was thermally evaporated under high vacuum ( $\approx 2 \times 10^{-7}$  mbar) to a total film thickness of 75 nm. Without breaking the vacuum, high purity (99.9999%) aluminum (Agar Scientific) was subsequently deposited to a thickness of 2 nm. The thin aluminum layer readily oxidizes into Al<sub>2</sub>O<sub>2</sub>, acting as a protective barrier towards the underlying silver.<sup>[71]</sup>

TEPL spectra were recorded using a 0.7 NA infinity corrected long working distance objective (Plan Apo, Mitutoyo) and 633 nm He Ne laser pump excitation. The collected light was dispersed and recorded with a Raman spectrometer (Labram HR Evolution, Horiba) using a 300 grooves mm<sup>-1</sup> grating. TEPL measurements were carried out in ambient conditions, with the sample being taken out of storage in inert glovebox conditions just prior to the measurement to reduce the impact of environmental adsorbates. Spectra were recorded in "dual spec" mode, where at each pixel separate spectra are recorded with intermittent and contact mode topography feedback. Given the different tip sample distances at each of the operation modes, subtracting the recorded TEPL spectrum at intermittent mode from the contact mode acquisition effectively removes the far-field component of the scattering signal from the tip-enhanced near-field component.<sup>[45]</sup>

# **Supporting Information**

Supporting Information is available from the Wiley Online Library or from the author.

# **Acknowledgements**

This project received funding from the European Union's Horizon 2020 research and innovation program under grant agreement GrapheneCore3 number 881603. The work was also financially supported by the UK government's Department for Business, Energy and Industrial Strategy (BEIS) through the National Measurement System. F.R., F.A.C., and S.W. acknowledge funding from the European Union's Horizon 2020 research and innovation program under the Marie Skłodowska-Curie Grant Agreement No. 721874 (SPM2.0). The authors would like to thank Dr. Sayanti Samaddar for providing helpful comments that improved the manuscript.

# **Conflict of Interest**

The authors declare no conflict of interest.

219910x, 2022, 9, Downloaded from https://onlinelibrary.wiley.com/doi/10.1002/aelm.202200196 by Test, Wiley Online Library on [31/10/2022]. See the Terms and Conditions (https://onlinelibrary.wiley.com/ems-and-conditions) on Wiley Online Library for rules of use; OA articles are governed by the applicable Creative Commons Licensea

www.advancedsciencenews.com



# **Data Availability Statement**

The data that support the findings of this study are available from the corresponding author upon reasonable request.

# **Keywords**

2D materials, Kelvin probe force microscopy, optoelectronics, Schottky barrier, tip-enhanced photoluminescence

Received: February 22, 2022 Revised: March 11, 2022 Published online: March 31, 2022

- [1] D. Jariwala, V. K. Sangwan, L. J. Lauhon, T. J. Marks, M. C. Hersam, *ACS Nano* **2014**, *8*, 1102.
- [2] A. Splendiani, L. Sun, Y. Zhang, T. Li, J. Kim, C. Y. Chim, G. Galli, F. Wang, Nano Lett. 2010, 10, 1271.
- [3] K. F. Mak, C. Lee, J. Hone, J. Shan, T. F. Heinz, Phys. Rev. Lett. 2010, 105, 136805.
- [4] W. Jin, P. C. Yeh, N. Zaki, D. Zhang, J. T. Sadowski, A. Al-Mahboob, A. M. Van Der Zande, D. A. Chenet, J. I. Dadap, I. P. Herman, P. Sutter, J. Hone, R. M. Osgood, *Phys. Rev. Lett.* 2013, 111, 106801.
- [5] S. Tongay, J. Zhou, C. Ataca, K. Lo, T. S. Matthews, J. Li, J. C. Grossman, J. Wu, Nano Lett. 2012, 12, 5576.
- [6] W. Zhao, Z. Ghorannevis, L. Chu, M. Toh, C. Kloc, P. H. Tan, G. Eda, ACS Nano 2013, 7, 791.
- [7] V. Podzorov, M. E. Gershenson, C. Kloc, R. Zeis, E. Bucher, Appl. Phys. Lett. 2004, 84, 3301.
- [8] W. Bao, X. Cai, D. Kim, K. Sridhara, M. S. Fuhrer, Appl. Phys. Lett. 2013, 102, 042104.
- [9] A. Daus, S. Vaziri, V. Chen, Ç. Köroğlu, R. W. Grady, C. S. Bailey, H. R. Lee, K. Schauble, K. Brenner, E. Pop, Nat. Electron. 2021, 4, 495
- [10] H. S. Lee, S. W. Min, Y. G. Chang, M. K. Park, T. Nam, H. Kim, J. H. Kim, S. Ryu, S. Im, *Nano Lett.* **2012**, *12*, 3695.
- [11] L. Zeng, L. Tao, C. Tang, B. Zhou, H. Long, Y. Chai, S. P. Lau, Y. H. Tsang, Sci. Rep. 2016, 6, 20343.
- [12] Z. Zheng, T. Zhang, J. Yao, Y. Zhang, J. Xu, G. Yang, Nanotechnology 2016, 27, 225501.
- [13] M. Bernardi, M. Palummo, J. C. Grossman, Nano Lett. 2013, 13, 3664
- [14] M. Fontana, T. Deppe, A. K. Boyd, M. Rinzan, A. Y. Liu, M. Paranjape, P. Barbara, Sci. Rep. 2013, 5, 12589.
- [15] D. Jariwala, A. R. Davoyan, J. Wong, H. A. Atwater, ACS Photonics 2017, 4, 2962.
- [16] C. Kim, I. Moon, D. Lee, M. S. Choi, F. Ahmed, S. Nam, Y. Cho, H. J. Shin, S. Park, W. J. Yoo, ACS Nano 2017, 11, 1588.
- [17] Y. Liu, J. Guo, E. Zhu, L. Liao, S. J. Lee, M. Ding, I. Shakir, V. Gambin, Y. Huang, X. Duan, *Nature* 2018, 557, 696.
- [18] X. Zhang, B. Liu, L. Gao, H. Yu, X. Liu, J. Du, J. Xiao, Y. Liu, L. Gu, Q. Liao, Z. Kang, Z. Zhang, Y. Zhang, Nat. Commun. 2021, 12, 1522.
- [19] A. Allain, J. Kang, K. Banerjee, A. Kis, Nat. Mater. 2015, 14, 1195.
- [20] S. Song, Y. Sim, S. Y. Kim, J. H. Kim, I. Oh, W. Na, D. H. Lee, J. Wang, S. Yan, Y. Liu, J. Kwak, J. H. Chen, H. Cheong, J. W. Yoo, Z. Lee, S. Y. Kwon, *Nat. Electron.* **2020**, *3*, 207.
- [21] L. Yu, Y.-H. Lee, X. Ling, E. J. G. Santos, Y. C. Shin, Y. Lin, M. Dubey, E. Kaxiras, J. Kong, H. Wang, T. Palacios, *Nano Lett.* 2014, 14, 3055.
- [22] S. Das, R. Gulotty, A. V. Sumant, A. Roelofs, Nano Lett. 2014, 14, 2861.
- [23] W. J. Yu, Z. Li, H. Zhou, Y. Chen, Y. Wang, Y. Huang, X. Duan, Nat. Mater. 2013, 12, 246.

- [24] Y. Sata, R. Moriya, S. Morikawa, N. Yabuki, S. Masubuchi, T. Machida, Appl. Phys. Lett. 2015, 107, 023109.
- [25] S. S. Chee, D. Seo, H. Kim, H. Jang, S. Lee, S. P. Moon, K. H. Lee, S. W. Kim, H. Choi, M. H. Ham, Adv. Mater. 2019, 31, 1804422.
- [26] W. J. Yu, Y. Liu, H. Zhou, A. Yin, Z. Li, Y. Huang, X. Duan, Nat. Nanotechnol. 2013, 8, 952.
- [27] S. W. LaGasse, P. Dhakras, K. Watanabe, T. Taniguchi, J. U. Lee, Adv. Mater. 2019, 31, 1901392.
- [28] Y. Ma, Y. Dai, M. Guo, C. Niu, B. Huang, Nanoscale 2011, 3, 3883.
- [29] C. Jin, F. A. Rasmussen, K. S. Thygesen, J. Phys. Chem. C 2015, 119, 19928.
- [30] S. S. Baik, S. Im, H. J. Choi, Sci. Rep. 2017, 7, 45546.
- [31] T. Le Quang, V. Cherkez, K. Nogajewski, M. Potemski, M. T. Dau, M. Jamet, P. Mallet, J. Y. Veuillen, 2D Mater. 2017, 4, 035019.
- [32] Y. J. Dappe, Y. Almadori, M. T. Dau, C. Vergnaud, M. Jamet, C. Paillet, T. Journot, B. Hyot, P. Pochet, B. Grévin, *Nanotechnology* 2020, 31, 255709.
- [33] S. Ulstrup, C. E. Giusca, J. A. Miwa, C. E. Sanders, A. Browning, P. Dudin, C. Cacho, O. Kazakova, D. K. Gaskill, R. L. Myers-Ward, T. Zhang, M. Terrones, P. Hofmann, *Nat. Commun.* 2019, 1, 3283.
- [34] S. Samaddar, I. Yudhistira, S. Adam, H. Courtois, C. B. Winkelmann, Phys. Rev. Lett. 2016, 116, 126804.
- [35] K. Nagashio, T. Yamashita, T. Nishimura, K. Kita, A. Toriumi, J. Appl. Phys. 2011, 110, 024513.
- [36] C. Melios, A. Centeno, A. Zurutuza, V. Panchal, C. E. Giusca, S. Spencer, S. R. P. Silva, O. Kazakova, *Carbon* 2016, 103, 273.
- [37] A. F. Rigosi, H. M. Hill, Y. Li, A. Chernikov, T. F. Heinz, Nano Lett. 2015, 15, 5033.
- [38] K. He, N. Kumar, L. Zhao, Z. Wang, K. F. Mak, H. Zhao, J. Shan, Phys. Rev. Lett. 2014, 113, 026803.
- [39] A. M. Jones, H. Yu, N. J. Ghimire, S. Wu, G. Aivazian, J. S. Ross, B. Zhao, J. Yan, D. G. Mandrus, D. Xiao, W. Yao, X. Xu, Nat. Nanotechnol. 2013, 8, 634.
- [40] M. Zhao, P. Song, J. Teng, ACS Appl. Mater. Interfaces 2018, 10, 44102.
- [41] C. E. Giusca, Z. Lin, M. Terrones, D. K. Gaskill, R. L. Myers-Ward, O. Kazakova, J. Phys. Mater. 2019, 2, 2.
- [42] L. Liu, H. Zhou, R. Cheng, W. J. Yu, Y. Liu, Y. Chen, J. Shaw, X. Zhong, Y. Huang, X. Duan, ACS Nano 2012, 6, 8241.
- [43] D. Ziegler, P. Gava, J. Güttinger, F. Molitor, L. Wirtz, M. Lazzeri, A. M. Saitta, A. Stemmer, F. Mauri, C. Stampfer, Phys. Rev. B: Condens. Matter Mater. Phys. 2011, 83, 235434.
- [44] P. T. T. Le, L. M. Bui, N. N. Hieu, H. V. Phuc, B. Amin, N. V. Hieu, C. V. Nguyen, *Diamond Relat. Mater.* 2019, 94, 129.
- [45] C. F. Wang, M. Zamkov, P. Z. El-Khoury, J. Phys. Chem. C 2021, 125, 12251
- [46] S. Seo, I. J. Park, M. Kim, S. Lee, C. Bae, H. S. Jung, N. G. Park, J. Y. Kim, H. Shin, *Nanoscale* 2016, 8, 11403.
- [47] N. Kumar, A. Zoladek-Lemanczyk, A. A. Y. Guilbert, W. Su, S. M. Tuladhar, T. Kirchartz, B. C. Schroeder, I. McCulloch, J. Nelson, D. Roy, F. A. Castro, *Nanoscale* 2017, 9, 272.
- [48] S. Samaddar, J. Coraux, S. C. Martin, B. Grévin, H. Courtois, C. B. Winkelmann, *Nanoscale* 2016, 8, 15162.
- [49] T. Wagner, D. Köhler, P. Milde, L. M. Eng, Appl. Phys. Lett. 2013, 103, 023102.
- [50] K. S. Novoselov, A. K. Geim, S. V. Morozov, D. Jiang, M. I. Katsnelson, I. V. Grigorieva, S. V. Dubonos, A. A. Firsov, *Nature* 2005, 438, 197.
- [51] Y. Zhang, Y. W. Tan, H. L. Stormer, P. Kim, Nature 2005, 438, 201.
- [52] Z. Q. Li, E. A. Henriksen, Z. Jiang, Z. Hao, M. C. Martin, P. Kim, H. L. Stormer, D. N. Basov, Nat. Phys. 2008.
- [53] S. Jung, G. M. Rutter, N. N. Klimov, D. B. Newell, I. Calizo, A. R. Hight-Walker, N. B. Zhitenev, J. A. Stroscio, Nat. Phys. 2011, 4, 532.





- [54] V. Panchal, R. Pearce, R. Yakimova, A. Tzalenchuk, O. Kazakova, Sci. Rep. 2013, 3, 2597.
- [55] E. G. Castanon, A. F. Scarioni, H. W. Schumacher, S. Spencer, R. Perry, J. A. Vicary, C. A. Clifford, H. Corte-León, J. Phys. Commun. 2020, 4, 095025.
- [56] A. Fabricius, A. Cultrera, A. Catanzaro, (unpublished).
- [57] C. Melios, N. Huang, L. Callegaro, A. Centeno, A. Cultrera, A. Cordon, V. Panchal, I. Arnedo, A. Redo-Sanchez, D. Etayo, M. Fernandez, A. Lopez, S. Rozhko, O. Txoperena, A. Zurutuza, O. Kazakova, Sci. Rep. 2020, 10, 3223.
- [58] Y. J. Yu, Y. Zhao, S. Ryu, L. E. Brus, K. S. Kim, P. Kim, Nano Lett. 2009, 9, 3430.
- [59] K. Zou, X. Hong, J. Zhu, Phys. Rev. B: Condens. Matter Mater. Phys. 2011, 84, 085408.
- [60] G. Giovannetti, P. A. Khomyakov, G. Brocks, V. M. Karpan, J. Van Den Brink, P. J. Kelly, Phys. Rev. Lett. 2008, 101, 026803.
- [61] Y. Li, J. Wang, B. Zhou, F. Wang, Y. Miao, J. Wei, B. Zhang, K. Zhang, Phys. Chem. Chem. Phys. 2018, 20, 24109.
- [62] M. Farmanbar, G. Brocks, Phys. Rev. B: Condens. Matter Mater. Phys. 2015, 91, 161304.

- [63] T. V. Vu, N. V. Hieu, H. V. Phuc, N. N. Hieu, H. D. Bui, M. Idrees, B. Amin, C. V. Nguyen, Appl. Surf. Sci. 2020, 507, 145036.
- [64] T. D. Ngo, M. Lee, Z. Yang, F. Ali, I. Moon, W. J. Yoo, Adv. Electron. Mater. 2020, 6, 2000616.
- [65] K. Murali, M. Dandu, K. Watanabe, T. Taniguchi, K. Majumdar, Adv. Funct. Mater. 2021, 31, 2010513.
- [66] P. Pacher, A. Lex, V. Proschek, H. Etschmaier, E. Tchernychova, M. Sezen, U. Scherf, W. Grogger, G. Trimmel, C. Slugovc, E. Zojer, Adv. Mater. 2008, 20, 3143.
- [67] X. Wang, Z. Zhang, J. Tang, B. Gao, W. Sun, F. Xu, H. Wu, H. Qian, AIP Adv. 2020, 10, 055203.
- [68] A. Castellanos-Gomez, M. Buscema, R. Molenaar, V. Singh, L. Janssen, H. S. J. Van Der Zant, G. A. Steele, 2D Mater. 2014, 1, 011002.
- [69] T. Wagner, H. Beyer, P. Reissner, P. Mensch, H. Riel, B. Gotsmann, A. Stemmer, Beilstein J. Nanotechnol. 2015, 6, 2193.
- [70] L. Nony, A. S. Foster, F. Bocquet, C. Loppacher, Phys. Rev. Lett. 2009, 103, 036802.
- [71] C. A. Barrios, A. V. Malkovskiy, A. M. Kisliuk, A. P. Sokolov, M. D. Foster, J. Phys. Chem. C 2009, 113, 8158.